Journal of
Materials Chemistry B

Accepted Manuscript

This is an *Accepted Manuscript*, which has been through the RSC Publishing peer review process and has been accepted for publication.

Accepted Manuscripts are published online shortly after acceptance, which is prior to technical editing, formatting and proof reading. This free service from RSC Publishing allows authors to make their results available to the community, in citable form, before publication of the edited article. This *Accepted Manuscript* will be replaced by the edited and formatted *Advance Article* as soon as this is available.

To cite this manuscript please use its permanent Digital Object Identifier (DOI®), which is identical for all formats of publication.

More information about *Accepted Manuscripts* can be found in the **Information for Authors**.

Please note that technical editing may introduce minor changes to the text and/or graphics contained in the manuscript submitted by the author(s) which may alter content, and that the standard **Terms & Conditions** and the **ethical guidelines** that apply to the journal are still applicable. In no event shall the RSC be held responsible for any errors or omissions in these *Accepted Manuscript* manuscripts or any consequences arising from the use of any information contained in them.

Cite this: DOI: 10.1039/c0xx00000x

www.rsc.org/xxxxxx

ARTICLE TYPE

Surface Functionalized Barium Sulfate Nanoparticles: Controlled *in situ* Synthesis and Application in Bone Cement

Chao Fang[1, 2], Ruixia Hou[1], Kefeng Zhou[3*], Feibin Hua[4], Yang Cong[4], Jianfeng Zhang[2], Jun Fu[1*], and Ya-Jun Cheng[1*]

Received (in XXX, XXX) Xth XXXXXXXXX 20XX, Accepted Xth XXXXXXXXX 20XX
DOI: 10.1039/b000000x

The controlled synthesis of surface functionalized $BaSO_4$ nanoparticles with the diameter below 50 nm is achieved by combining the *in situ* generation of SO_4^{2-} and the use of difunctional surface modification agent of (2-(Methacryloyloxy) ethyl dimethyl-(3-sulfopropyl) ammonium hydroxide (MSAH). Particularly, a pre-decomposition process of the SO_4^{2-} precursor ($S_2O_8^{2-}$) is applied to decouple the *in situ* generation of SO_4^{2-} and precipitation of $BaSO_4$. As a result, the nucleation and growth of $BaSO_4$ particles is manipulated, which significantly reduces the particle size. Different combinations of the pre-decomposition time and MSAH/$BaCl_2$ molar ratios showed remarkable influence on the morphology and surface functionality of the $BaSO_4$ particles. Furthermore, the morphology control by using other difunctional surface modification agents e.g 3-Sulfopropyl methacrylate potassium salt (SMPS) and 2-Acrylamido-2-Methylpropane Sulfonic Acid (AMSA) is examined. The MSAH-functionalized $BaSO_4$ nanoparticles used as filler in bone cements effectively improved the bending modulus and compressive strength of the PMMA bone cements. The bone cement with MSAH-functionalized $BaSO_4$ nanoparticles exhibited good radiopacity. Moreover, in vitro cell culture experiments demonstrated improved biocompatibility compared to bare $BaSO_4$ particles. The MSAH-functionalized $BaSO_4$ nanoparticles may be ideal candidate material as bone cement filler.

Introduction

Barium sulfate ($BaSO_4$) nanoparticles have found wide applications in catalyst carrier[1, 2], biomedical devices[3], engineering plastics[4] and adsorbent materials[5, 6] due to their excellent stability and inertness, high specific gravity, and outstanding optical properties[7-10]. Particularly, $BaSO_4$ has been extensively used as filler and radiopacifier in PMMA-based bone cement to improve the fixation of artificial joint and facilitate the post-operation tracking of joint replacement surgery.

Although the PMMA bone cement has achieved great clinical success, the use of $BaSO_4$ particles in bone cement causes detrimental side effects. As inorganic filler, $BaSO_4$ particles have poor compatibility and weak interaction with the PMMA matrix and tend to agglomerate and phase separate from the PMMA matrix. As a result, the mechanical properties and corresponding clinical performance of the bone cements are deteriorated[11-18]. The morphology and surface functionality of $BaSO_4$ particles are critical for the properties of the bone cements. Nano-sized $BaSO_4$ particles are reported to improve the mechanical properties of bone cements effectively[10, 19-25]. Because the $BaSO_4$ nanoparticles tend to agglomerate within the PMMA matrix, surface modification of the $BaSO_4$ nanoparticles is critical to improve the compatibility and interactions between the $BaSO_4$ nanoparticles and the PMMA matrix. Therefore, it is essential to develop a reliable strategy to control the morphology and surface functionality of the $BaSO_4$ nanoparticles simultaneously.

Various surface modification agents have been utilized to tune the morphology and surface functionality of the $BaSO_4$ particles, including organic acids[26, 27], amines[28], methacrylates[21], octadecyl dihydrogen phosphates[29], and copolymers[30, 31]. These agents usually form moderate coordination bonds with Ba^{2+} or possess weak non-covalent interactions with the PMMA matrix. The potential of using such agents to tune the morphology and surface functionality of $BaSO_4$ is limited. Moreover, most synthetic routes of $BaSO_4$ are based on the direct mixing of Ba^{2+} and SO_4^{2-}. The formation of $BaSO_4$ is rapid and violent, making it difficult to control the nucleation and growth of $BaSO_4$ particles. To address this issue, *in situ* generation of SO_4^{2-} via γ-irradiation was developed. By coupling the chelating agent of EDTA for Ba^{2+}, mesoporous $BaSO_4$ microspheres were synthesized[32-34]. Nevertheless, this process has a few disadvantages. First, this process is not facile because γ-irradiation is not routinely accessible for most laboratories. Second, EDTA has a poor compatibility and weak interaction with the PMMA matrix. Third, the $BaSO_4$ particles modified with EDTA are not suitable for biomedical use since EDTA is toxic.

In our previous work, a new strategy to achieve the controlled synthesis of surface functionalized $BaSO_4$ nanoparticles under mild condition was developed[35]. *In situ* generation of SO_4^{2-} is realized by thermal decomposition of $K_2S_2O_8$ in aqueous basic solution. Besides, a difunctional molecule of 2-(Methacryloyloxy) ethyl dimethyl-(3-sulfopropyl) ammonium hydroxide (MSAH) was used as surface modification agent. The sulfonate group of MSAH coordinates with Ba^{2+}, while the methacrylate group can copolymerize with MMA monomer during bone cement curing. The $BaSO_4$ particle size can be well controlled by tuning the molar ratio between MSAH

and $BaCl_2$. Compared to the conventional μm-sized $BaSO_4$ particles, the MSAH-functionalized $BaSO_4$ nanoparticles effectively improve the compressive and bending strength of the bone cements[35].

Despite the success of this strategy, a few critical issues remain to be addressed. First, the average size of the MSAH-functionalized $BaSO_4$ nanoparticles needs to be further reduced, which is supposed to endow bone cement with better mechanical properties. Instead of the one-pot fashion of simultaneous *in situ* generation of SO_4^{2-} and precipitation of $BaSO_4$, in this work, the decomposition-precipitation process is decoupled (**Scheme 1**). A pre-decomposition process of $K_2S_2O_8$ is applied, which introduces free SO_4^{2-} in solution. The modified strategy provides more possibilities to manipulate the nucleation and growth of the $BaSO_4$ nanoparticles. Second, the general applicability of the strategy using surface modification agents other than MSAH to control the morphology and surface functionality of $BaSO_4$ needs to be examined. 3-Sulfopropyl methacrylate potassium salt (SMPS), and 2-Acrylamido-2-Methylpropane Sulfonic Acid (AMSA) are used as surface modification agents (**Scheme 2**). Similar to MSAH, they are also supposed to form strong coordination bonds with Ba^{2+} and copolymerize with MMA monomer during bone cement curing. The effects of SMPS and AMSA on the morphology and surface functionality control of $BaSO_4$ are investigated. Third, the effects of particle size and surface functionality of $BaSO_4$ on the biocompatibility of the PMMA bone cements needs to be established before the bone cements can be seriously considered for practical applications. The *in vitro* biocompatibility of the bone cements containing surface functionalized $BaSO_4$ nanoparticles are evaluated by characterizing the adsorption and proliferation behavior of human osteoblast cells on the surface of the bone cements.

Experimental

Materials

$K_2S_2O_8$ (Aladdin, 99.5%), $BaCl_2 \cdot H_2O$ (Alfa Aesar, 99%), 2-(Methacryloyloxy) ethyl dimethyl-(3-sulfopropyl) ammonium hydroxide (MSAH, Aldrich, 98%), 3-Sulfopropyl methacrylate potassium salt (SMPS, Aldrich, 98%), 2-Acrylamido-2-Methylpropane Sulfonic Acid (AMSA, Aldrich, 98%) and KOH (Sinopharm, 98%) were used as received. De-ionized water was used as solvent. Methyl methacrylate (MMA), Dimethyl-*beta*-Propiothetin hydrochloride (DMPT), hydroquinone (HQ), Benzoyl peroxide (BPO) and biomedical grade poly (methyl methacrylate) (PMMA) were purchased from Tianjin Institute of Synthetic Materials Industry and used as received.

In Situ Synthesis of Surface Functionalized $BaSO_4$ Nanoparticles

The KOH-$K_2S_2O_8$ solution was prepared by mixing 200 mL of 0.25 mol/L $K_2S_2O_8$ solutions with 50 mL of 0.5 mol/L KOH solution. This solution was heated at 90 °C for 0 min to 240 min (pre-decomposition process) with continuous stirring, followed by cooling in water at room temperature for 30 min. Taking MSAH as an example, 200 mL of 0.25 mol/L $BaCl_2$ aqueous solution was added to the aqueous solution of MSAH with the final MSAH/$BaCl_2$ molar ratio varied between 0 and 0.128. Then the cooled KOH-$K_2S_2O_8$ solution was added dropwise to the $BaCl_2$-KOH-MSAH solution within 1 min at 60 °C and stirring at 400 rpm. The reaction was carried out until the pH reached around 7. The obtained precipitates were separated from the solution by centrifugation and washing with de-ionized water for three times, followed by vacuum-drying at 60 °C for 24 hours. The $BaSO_4$ nanoparticles functionalized with SMPS and AMSA were synthesized in the same way as the MSAH-functionalized $BaSO_4$ nanoparticles.

Preparation of Bone Cement

Bone cements were prepared by mixing the liquid component with the solid component at room temperature (25 °C). The solid component consisted of micro PMMA beads, benzoyl peroxide (BPO) and the surface-functionalized $BaSO_4$ nanoparticles (mass ratio of $BaSO_4$ over total amount of sample: 0, 5 %, 10 %, and 20 %). The liquid component consisted of MMA (as base monomer), DMPT (accelerator) and HQ (inhibitor). The mass ratio of the solid component against the liquid component was kept at 2 in all bone cement samples. All of the bone cement samples were prepared by hand mixing without vacuum evacuation.

Scanning Electron Microscope (SEM)

The morphology of the surface-functionalized $BaSO_4$ nanoparticles was characterized by S4800 scanning electron microscope (SEM, Tokyo, Japan) with an accelerating voltage of 15.0 kV. Gold sputtering was applied before imaging.

X-Ray Diffraction (XRD)

The crystallographic phase of the surface functionalized $BaSO_4$ nanoparticles was identified using X-ray diffraction (XRD) (Bruker AXS D8 Advance, λ=1.541 Å, 2.2 kW) with θ ranged between 20 ° and 70 °.

Fourier-Transform Infrared (FTIR) Spectroscopy

The surface-modified $BaSO_4$ nanoparticles were investigated using Fourier-transform infrared (FTIR) spectrometer. Solid KBr pellet samples were prepared and scanned on a Nicolet 6700 spectrometer (Thermal Fisher, Madison, Wisconsin) from 4000 cm^{-1} to 400 cm^{-1} with 4 cm^{-1} resolution for 32 scans each.

Thermo Gravimetric Analysis (TGA)

The amount of the surface modification agent on $BaSO_4$ nanoparticles was quantified by thermo gravimetric analyzer (TGA/DSC1, Mettler Toledo, Switzerland). The temperature range was set between 50 °C and 800 °C with a ramp rate of 20 °C/min.

Mechanical Tests

Cuboid $BaSO_4$ samples (approximately 75 mm × 10 mm × 3.3 mm) were prepared according to ISO5833:2002 and tested in bending mode using an Instron 5567 mechanical testing machine (Instron, Boston, MA) at a crosshead speed of 5.0 mm/min. Five. samples were tested for each set of sample (n=5) at a crosshead speed of 5.0 mm/min. Cylindrical $BaSO_4$ samples (approximately 6 mm in diameter and 12 mm in height) were tested in unconfined compressive mode at a crosshead speed of 20.0 mm/min. The compression limit was set at 90 % strain to protect

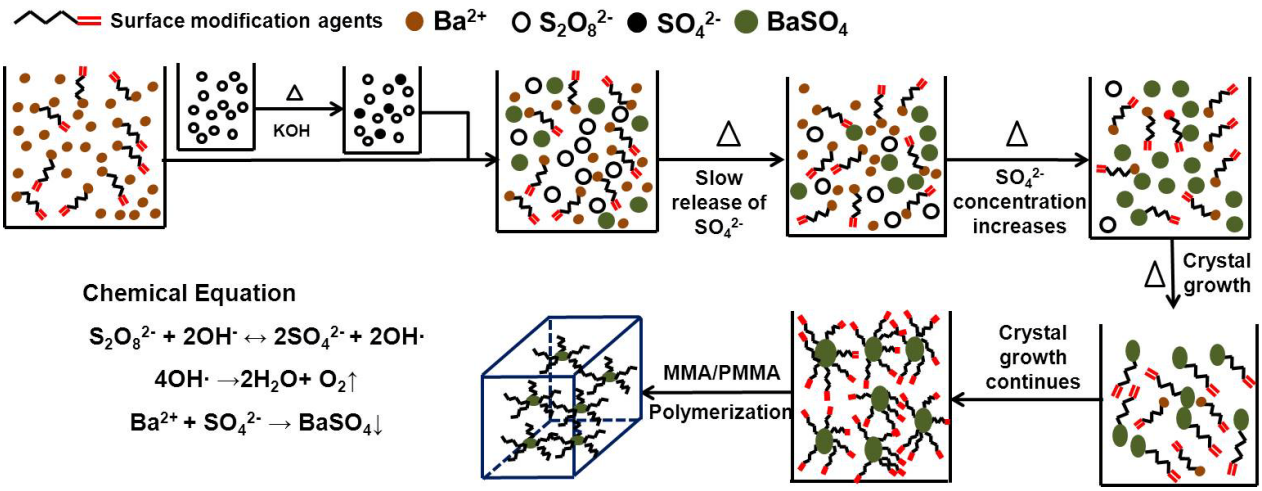

Scheme 1. Scheme of the controlled in situ synthesis of surface functionalized $BaSO_4$ nanoparticles and subsequent fabrication of the acrylic bone cement.

the load cell. Five specimens were tested for each material (n=5).

X-Ray Radiopacity Characterization

Cubic samples (approximately 10 mm × 15 mm × 3.3 mm) were exposed to x-ray scan using an x-ray Generator (Philips Optimus 65, Japan, 66 kV, 6Mas, in air, exposure time 15.8 Ms). Images were recorded and the transmitted signal was analysed using Firax Workstation.

In Vitro Cell Culture

Human SV40 osteoblasts (hFOB 1.19, Shanghai Institute of Life Sciences, Cell Resource Center, Chinese Academy of Sciences) at passage 5 were seeded at 1.4×10^5 cells/ml on sterilized cured bone cement samples (10 mm long and 4.6 mm wide) in 48-well plates (Corning) (n=4 each). The samples were removed from the culture media after one day and washed with PBS. Then the samples were fixed with glutaraldehyde (2.5 vol. %). After washed with PBS, 10 μg/ml of 4', 6-diamidino-2-phenylindole (DAPI, Invitrogen) was added and the samples were incubated in darkness at room temperature for 5 min, followed by washing with PBS for three times. Finally, the samples were imaged using confocal laser scanning microscope (CLSM, Leica TCS SP5 II, Braunschweig, Germany).

The osteoblast cells on the samples were also quantitatively investigated by CCK-8 assay after culture for one day. 200 μl of the reaction solution was put into 96-well plates and the optical density at 450 nm of each well was read by SpectraMax 190 microplate reader (Molecular Devices, Sunnyvale, California, USA).

Results and Discussion

Controlled *in situ* Synthesis of Surface functionalized $BaSO_4$ Nanoparticles

The controlled *in situ* synthesis of surface-functionalized $BaSO_4$ nanoparticles and fabrication of PMMA bone cement is described in **Scheme 1**. Generally, *in situ* generation of SO_4^{2-} via thermal decomposition of $K_2S_2O_8$ in basic aqueous solution is combined with difunctional surface modification agent containing both sulfonate group and methacrylate group (**Scheme 2**). Instead of the one-pot synthesis of surface functionalized $BaSO_4$ nanoparticles[30], herein, the *in situ* generation of SO_4^{2-} and formation of $BaSO_4$ are decoupled. The pre-decomposition of $K_2S_2O_8$ into SO_4^{2-} is applied before the two precursor solutions are mixed. The pH of the solutions decreases over reaction time, indicating the generation of SO_4^{2-} before and after solution mixing (**Figure S1**). The free SO_4^{2-} induces the formation of more $BaSO_4$ nuclei upon solution mixing. Consequently, the number of $BaSO_4$ nanoparticles formed in solution is increased and the average particle size is changed.

Morphology Control of the MSAH functionalized $BaSO_4$ Particles

The combined effects of both the pre-decomposition time of $K_2S_2O_8$ and molar ratio of MSAH/$BaCl_2$ on the morphology of the $BaSO_4$ particles are systematically investigated. The pre-decomposition time determines the amount of free SO_4^{2-} generated in solution, which plays an important role in the nucleation and growth of $BaSO_4$ particles. The molar ratio of MSAH/$BaCl_2$ influences the morphology of the $BaSO_4$ particles. According to the pH evolution over time (**Figure S1**), the solution reaches neutral after *ca.* 5 hours, implying the completion of the decomposition. Therefore, the pre-decomposition time is varied between 0 and 5 hours.

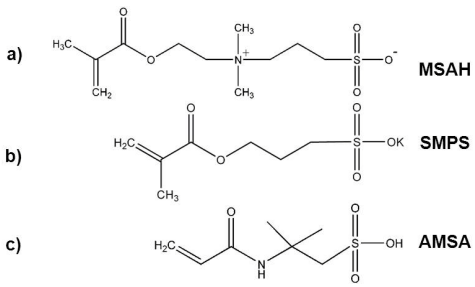

Scheme 2. Molecular structures of the surface modification agents. a: (2-(Methacryloyloxy) ethyl dimethyl-(3-sulfopropyl) ammonium hydroxide (MSAH), b: 3-Sulfopropyl methacrylate potassium salt (SMPS), c: 2-Acrylamido-2-Methyl- propane Sulfonic Acid (AMSA).

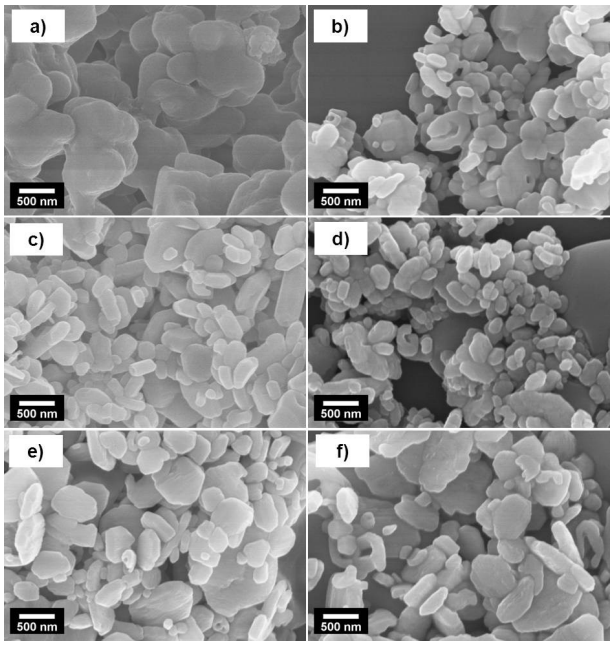

Figure 1. SEM images of the MSAH-functionalized $BaSO_4$ particles synthesized with the molar ratio of MSAH/$BaCl_2$ of 0 and a series of pre-decomposition time (a: 0 min, b: 15 min, c: 30 min, d: 60 min, e: 120 min, f: 240 min).

The molar ratio of MSAH/$BaCl_2$ is set between 0 and 0.128 referring to our previous work[35].

Morphology Control of the MSAH functionalized $BaSO_4$ Particles

The combined effects of both the pre-decomposition time of $K_2S_2O_8$ and molar ratio of MSAH/$BaCl_2$ on the morphology of the $BaSO_4$ particles are systematically investigated. The pre-decomposition time determines the amount of free SO_4^{2-} generated in solution, which plays an important role in the nucleation and growth of $BaSO_4$ particles. The molar ratio of MSAH/$BaCl_2$ influences the morphology of the $BaSO_4$ particles. According to the pH evolution over time (**Figure S1**), the solution reaches neutral after *ca*. 5 hours, implying the completion of the decomposition. Therefore, the pre-decomposition time is varied between 0 and 5 hours. The molar ratio of MSAH/$BaCl_2$ is set between 0 and 0.128 referring to our previous work[35].

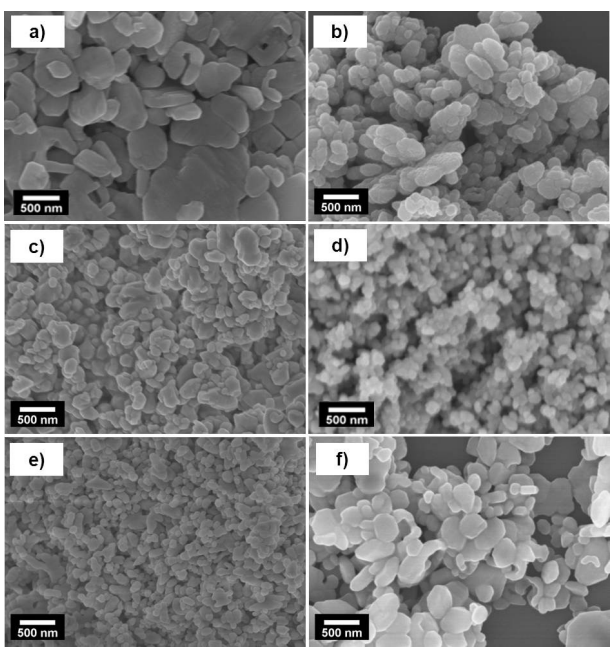

Figure 2. SEM images of the MSAH-functionalized $BaSO_4$ particles synthesized with the molar ratio of MSAH/$BaCl_2$ of 0.008 and a series of pre-decomposition time (a: 0 min, b: 15 min, c: 30 min, d: 60 min, e: 120 min, f: 240 min).

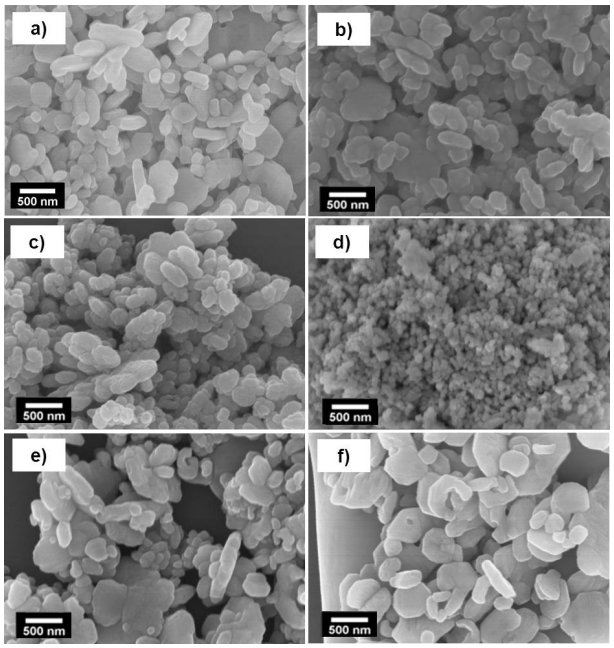

Figure 3. SEM images of the MSAH-functionalized $BaSO_4$ nanoparticles synthesized with different pre-decomposition time (molar ratio of MSAH/$BaCl_2$: 0.016, pre-decomposition time: a: 0 min, b: 15 min, c: 30 min, d: 60 min, e: 120 min, f: 240 min).

The morphology of the $BaSO_4$ particles synthesized with different combinations of pre-decomposition time and MSAH/$BaCl_2$ molar ratio are systematically presented in **Figures 1-6** and **Table 1**. The morphology of the $BaSO_4$ particles synthesized without MSAH do not show obvious changes from 0 to 240 min (Figure 1 and Table 1). However, when the molar ratio is gradually increased, the morphology of the synthesized $BaSO_4$ particles changes along with increased pre-decomposition time.

With the MSAH/$BaCl_2$ molar ratio of 0.008, the morphology of the particles changes significantly with increasing pre-decomposition time (Figure 2 and Table 1). At 0 and 15 min, platelet-like particles larger than 200 nm are formed. However, at 30, 60, and 120 min, spherical particles with smaller sizes (50 - 200 nm for 30 min, *ca*. 50 nm for 60 min, and 50 - 100 nm for 120 min) are formed. At 240 min, platelet-like particles appear again with the size between 100 and 300 nm.

With the MSAH/$BaCl_2$ molar ratio of 0.016, at 0 min, the particles are spheres or platelets with a broad size distribution from *ca*.100 to 500 nm (Figure 3a). At 15 and 30 min, the particle sizes remain between *ca*. 100 nm and 400 nm (Figure 3b and 3c). At 60 min, however, the particles become spherical and the average size is significantly reduced to about 30 nm (Figure 3d).

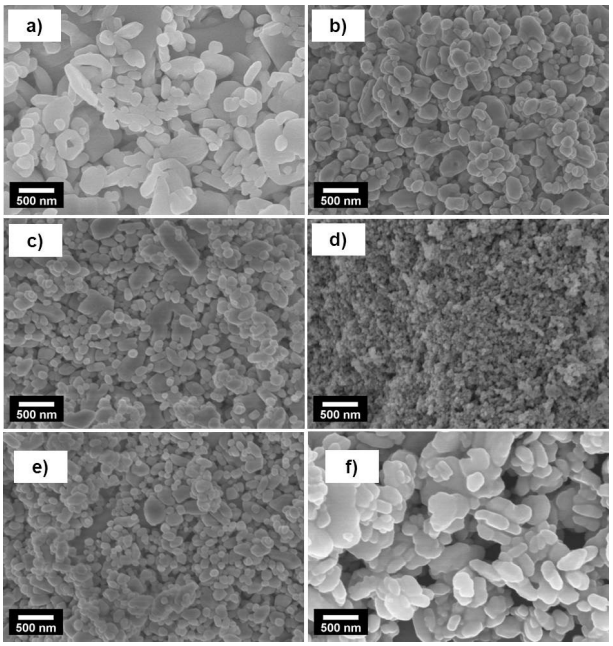

Figure 4. SEM images of the MSAH-functionalized $BaSO_4$ particles synthesized with the molar ratio of MSAH/$BaCl_2$ of 0.032 and different pre-decomposition time (a: 0 min, b: 15 min, c: 30 min, d: 60 min, e: 120 min, f: 240 min).

At 120 min, platelet-like particles appear with a broad size distribution from *ca*. 100 nm to 1 μm (Figure 3e). At 240 min, the average particle size is further increased to the range of 300 nm to 1 μm (Figure 3f).

With the molar ratio further increased to 0.032 and 0.064, the trend of the morphology evolution does not change significantly compared to the MSAH/$BaCl_2$ molar ratios of 0.008 and 0.016 (Figure 4, Figure 5, and Table 1).

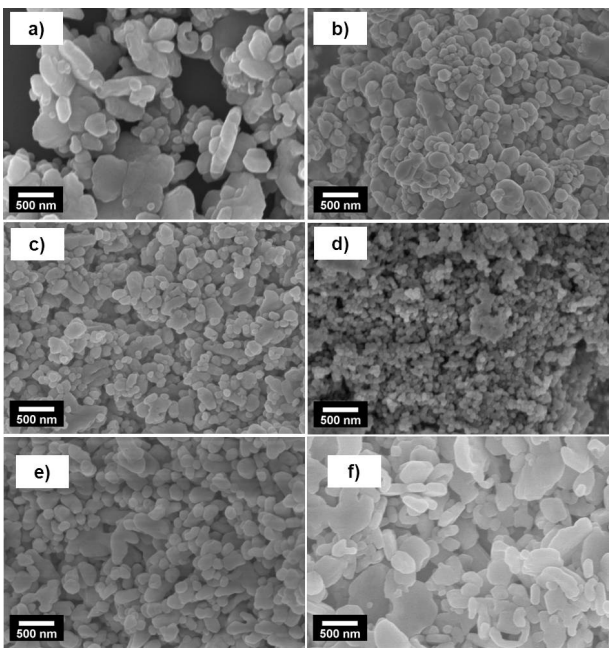

Figure 5. SEM images of the MSAH-functionalized $BaSO_4$ particles synthesized with the molar ratio of MSAH/$BaCl_2$ of 0.064 and different pre-decomposition time (a: 0 min, b: 15 min, c: 30 min, d: 60 min, e: 120 min, f: 240 min).

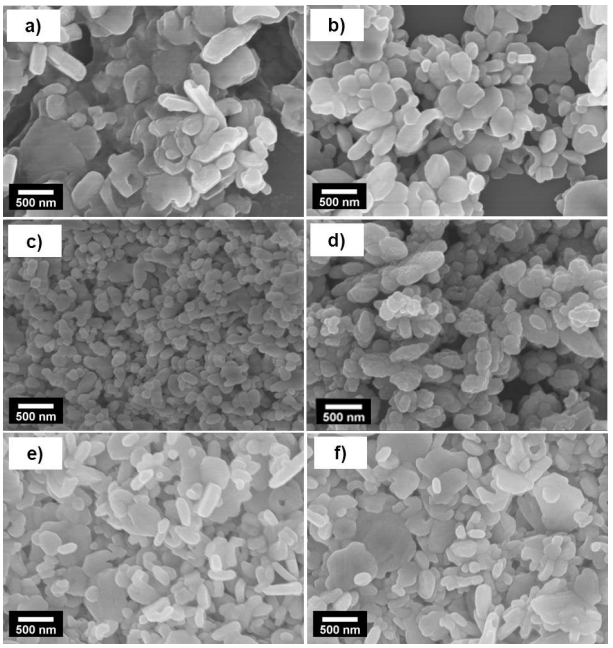

Figure 6. SEM images of the MSAH-functionalized $BaSO_4$ particles synthesized with the molar ratio of MSAH/$BaCl_2$ of 0.128 and different pre-decomposition time (a: 0 min, b: 15 min, c: 30 min, d: 60 min, e: 120 min, f: 240 min).

Without pre-decomposition, platelet-like particles are formed coexisting with small amount of spherical particles. With the pre-decomposition time extended to 15 min and 30 min, platelet-like and spherical particles are still observed, but the size is reduced to around 100 nm. With the pre-decomposition time of 60 min, uniform spherical particles are formed with the size decreased to around 10 nm (Figure 4d, molar ratio: 0.032) and 20 nm (Figure 5d, molar ratio: 0.064). When the pre-decomposition time is further increased to 120 min, besides the spherical particles, platelet-like particles appear, and the size of the particles is increased to above 100 nm. When the pre-decomposition time is increased to 240 min, platelet-like particles with the size of hundreds nanometres are formed again.

When the molar ratio is increased to 0.128, the morphology with respect to the pre-decomposition time is different (Figure 6 and Table 1). At 0 and 15 min, platelet-like particles with the size of hundreds of nanometres are formed. At 30 and 60 min, spherical particles coexist with platelet-like particles and the size is decreased to 100 - 300 nm. However, with the pre-decomposition time further increased to 120, and 240 min, large-sized platelet-like particles are predominantly formed. Considering that the pre-decomposition time of 60 min is mainly the morphology transition point with respect to different MSAH/$BaCl_2$ molar ratios, the morphologies of the particles synthesized with the pre-decomposition time of 60 min and a series of different MSAH/$BaCl_2$ molar ratios are further summarized in **Figure 7**. The particles without MSAH are sphere or platelet with a broad size distribution from about 100 nm to 500 nm (Figure 7a). When the MSAH/$BaCl_2$ molar ratio is increased to 0.008, the particles are of uniform sphere and the size is significantly decreased to about 50 nm (Figure 7b). As the molar ratio is increased to 0.016, 0.032, and 0.064, the particle size is further decreased to about 30 nm (Figure 7c), 10 nm

Cite this: DOI: 10.1039/c0xx00000x

www.rsc.org/xxxxxx

ARTICLE TYPE

Table 1. Shape and size of $BaSO_4$ particles synthesized with different pre-decomposition time and molar ratios of MSAH/$BaCl_2$. s: sphere, p: platelet-like.

Molar ratio of MSAH/$BaCl_2$ \ Pre-decomposition time (min)		0	15	30	60	120	240
0	average size (μm)	>1(p)	0.1-1(p)	0.1-0.5(p)	0.1-0.5(p)	0.1-0.5(p)	0.1-0.5(p)
0.008	average size (μm)	0.2-1(p)	0.2-0.3(p)	**0.05-0.2**(s)	**0.05**(s)	**0.05-0.1**(s)	0.1-0.3(p)
0.016	average size (μm)	0.1-0.5(p)	0.1-0.4(p)	0.1-0.3(p/s)	**0.03**(s)	0.1-1(p)	0.3-1(p)
0.032	average size (μm)	0.2-0.5(p)	0.1-0.2(p/s)	0.1-0.2(p/s)	**0.01**(s)	0.1-0.3(p/s)	0.3-1(p)
0.064	average size (μm)	0.3-1(p)	0.1-0.3(p/s)	0.1-0.3(p/s)	**0.02**(s)	0.1-0.4(p/s)	0.1-1(p)
0.128	average size (μm)	0.5-2(p)	0.3-0.5(p)	0.1-0.3(p/s)	0.1-0.3(p/s)	0.1-0.5(p)	0.2-2(p)

(Figure 7d), and inversely increased to around 20 nm (Figure 7e) respectively. However, when the molar ratio is extended to 0.128, the size of the particles is increased to the range between 100 nm and 300 nm. Both sphere and platelet-like particles are formed (Figure 7f). The results imply that MSAH exercise an effective morphology control over the $BasO_4$ particles. Particularly, with the pre-decomposition time fixed at 60 min, the particle size is significantly reduced to below 50 nm with the molar ratio of MSAH/$BaCl_2$ varied between 0.008 and 0.064.

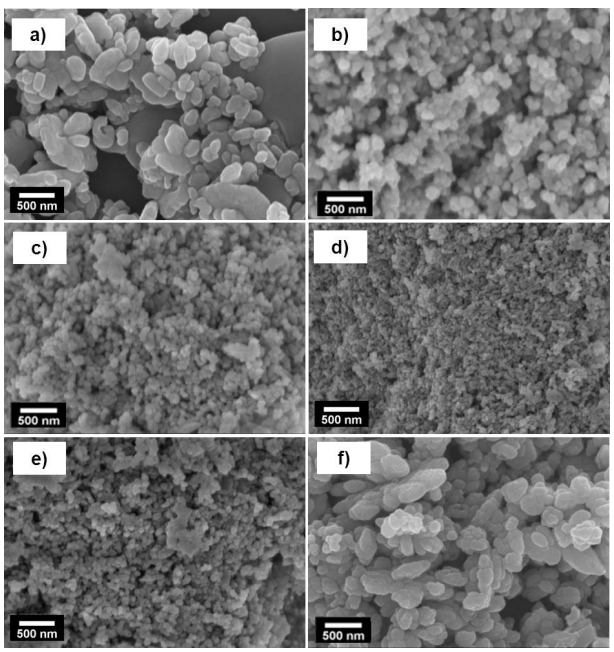

Figure 7. SEM images of the MSAH-functionalized $BaSO_4$ nanoparticles synthesized with the pre-decomposition time of 60 min and different molar ratios of MSAH/$BaCl_2$ (molar ratio of MSAH/$BaCl_2$: a: 0, b: 0.008, c: 0.016, d: 0.032, e: 0.064, f: 0.128).

By comparing the morphologies of the particles synthesized with the combinations of different MSAH/$BaCl_2$ molar ratios and pre-decomposition time, a few brief conclusions can be made. First, the size of the particles is successfully reduced to below 50 nm by the decoupled decomposition-precipitation strategy. Second, with different pre-decomposition time and fixed molar ratio, the particle size decreases first, followed by inverse increase. The morphology transition occurs at the pre-decomposition time of 60 min, where uniform spherical particles with the smallest size are formed (except the molar ratio of 0 and 0.128). Third, concerning the particles synthesized with different. molar ratios and fixed pre-decomposition time of 60 minutes, the particle size decreases significantly when MSAH is used as surface modification agent and particle size is reduced to below50 nm with the molar ratio less than 0.064. The particle size deceases with increasing molar ratio from 0.008 to 0.032, followed by inverse increase with further increased molar ratio to 0.064 and 0.128.

The morphology change of the particles synthesized with different MSAH/$BaCl_2$ molar ratio and fixed pre-decomposition time is due to the competition between nuclei formation and particle growth. In the MSAH-$BaCl_2$ solution, part of Ba^{2+} is bonded with MSAH via coordination bond and electrostatic interaction; while the remaining Ba^{2+} still keeps free in solution. In the KOH-$S_2O_8^{2-}$ solution, part of $S_2O_8^{2-}$ is decomposed into SO_4^{2-} during pre-decomposition; while part of $S_2O_8^{2-}$ still remains intact. Once the KOH-$S_2O_8^{2-}$ solution is mixed with the MSAH-$BaCl_2$ solution, the pre-formed free SO_4^{2-} forms coordination bonds with the free Ba^{2+}, rather than the Ba^{2+} already coordinated with MSAH. As a result, $BaSO_4$ nuclei are formed, which induce the growth of $BaSO_4$ particles. The particles continue to grow along with further *in situ* decomposition of $S_2O_8^{2-}$. The solution is lack of SO_4^{2-} due to the slow decomposition of $S_2O_8^{2-}$ and quick consumption of SO_4^{2-}. As a result, the Ba^{2+} on the surface of the particles prefers to coordinate with the sulfonate group of MSAH

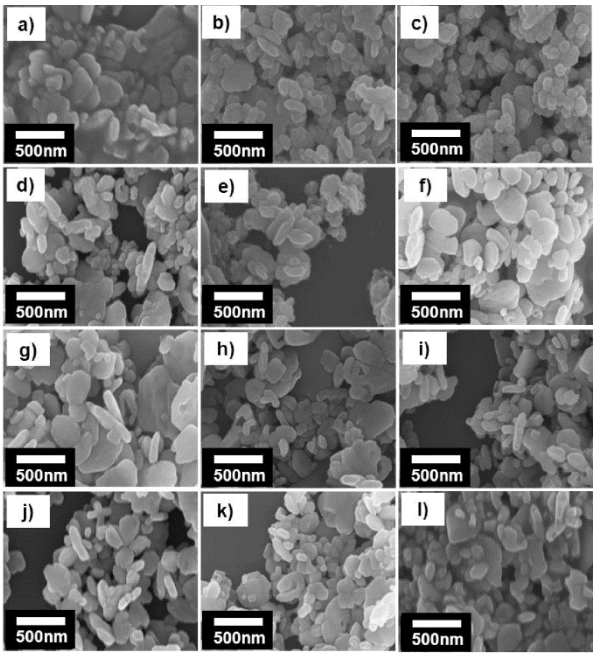

Figure 8. SEM images of the SMPS-coated BaSO4 particles synthesized with different pre-decomposition time(a: 0 min, b: 15 min, c: 30 min, d: 60 min, e: 120 min, f: 240 min, molar ratio of SMPS/$BaCl_2$: 0.016) and with different molar ratios of SMPS/$BaCl_2$ (g: 0, h: 0.008, i: 0.016, j: 0.032, k: 0.064, l: 0.128, pre-decomposition time: 60 min).

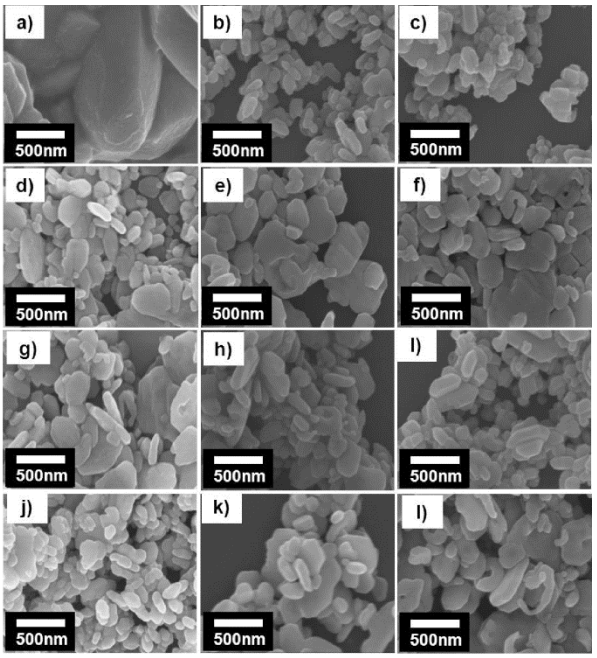

Figure 9. SEM images of the AMSA-coated $BaSO_4$ particles synthesized with different pre-decomposition time (a: 0 min, b: 15 min, c: 30 min, d: 60 min, e: 120 min, f: 240 min, molar ratio of AMSA/$BaCl_2$: 0.016) and with different molar ratios of AMSA/$BaCl_2$ (g: 0, h: 0.008, i: 0.016, j: 0.032, k: 0.064, l: 0.128, pre-decomposition time: 60 min).

rather than the deficient SO_4^{2-} in solution. Consequently, the surface of the particles is gradually decorated with MSAH. However, the growth of the particles will be inhibited to some extent with the MSAH decoration due to the following reasons. First, electrical shield layer around the particles will be formed as MSAH contains both negatively and positively charged functional groups. And the electrical shield layer will inhibit the anchor of Ba^{2+} ions onto the surface of the particles. Second, the adsorption of the hydrophilic solvated Ba^{2+} onto the particle surface will be inhibited by the hydrophobic methacrylate group of MSAH. Third, the steric hindrance caused by MSAH coating hinders further adsorption of solvated ions. As a result, with increasing amount of MSAH, the size of the particles is decreased. However, when the amount of MSAH in solution is increased to an excessive value, the amount of free Ba^{2+} in solution remains thimbleful and most of the fresh SO_4^{2-} can only coordinate with the MSAH-coordinated Ba^{2+} or MSAH-functionalized $BaSO_4$ nanoparticles. So the fresh SO_4^{2-} will promote the growth of the MSAH-functionalized $BaSO_4$, rather than form new $BaSO_4$ nuclei. Consequently, the average particle size is increased.

Morphology of the $BaSO_4$ Particles Functionalized with SMPS and AMSA

The applicability of other difunctional surface modification agents on the morphology control of the surface functionalized $BaSO_4$ is examined. 3-Sulfopropyl methacrylate potassium salt (SMPS), and 2-Acrylamido-2-Methylpropane Sulfonic Acid (AMSA) are used as surface modification agents (Scheme 2). **Figure 8** shows the SEM images of the SMPS functionalized $BaSO_4$ particles with different pre-decomposition times (Figure 8a-f) and different molar ratios of SMPS/$BaCl_2$ (Figure 8g-i). Without pre-decomposition, both spherical and platelet-like $BaSO_4$ particles are formed with a broad size distribution from *ca.* 200 nm to 500 nm (Figure 8a). When the pre-decomposition time is increased to 15 minutes, the morphology of the particles become much more uniform and the size is decreased to about 200 nm – 300 nm (Figure 8b). With the pre-decomposition time increased to 30 min (Figure 8c), 60 min (Figure 8d), and 120 min (Figure 8e), the morphology of the particles do not change significantly. However, with the pre-decomposition time of 240 min, the size of the $BaSO_4$ particles increases to 200 - 500 nm. Concerning the $BaSO_4$ particles synthesized with the pre-decomposition time of 60 min and different SMPS/$BaCl_2$ molar ratios, the particles synthesized without SMPS are platelet-like with a broad size distribution from about 250 to 500 nm (Figure 8g). The size of the particles is decreased to about 200 - 300 nm with the SMPS/$BaCl_2$ molar ratio of 0.008. With further increased molar ratio to 0.016, 0.032, and 0.064, the morphology of the particles do not change significantly (Figure 8h-8k). With the molar ratio increased to 0.128, the particle size increases to 300 - 500 nm.

The morphologies of the AMSA functionalized $BaSO_4$ particles synthesized different combinations of pre-decomposition time and AMSA/$BaCl_2$ molar ratios are exhibited in **Figure 9**. With molar ratio fixed at 0.016, μm-sized particles are formed without pre-decomposition (Figure 9a). However, as the pre-decomposition time increases to 15, 30 and 60 minutes, the particle size is effectively decreased to the range between 150 and 300 nm (Figure 9b-d). With the pre-decomposition time reached 120 and 240 minutes, the particle size increases to about 300 – 500 nm (Figure 9e-9f).

Concerning the AMSA-coated $BaSO_4$ particles synthesized with the pre-decomposition time of 60 min and different AMSA/$BaCl_2$ molar ratios, the particles synthesized without

Table 2. Mass loss (100°C -700°C by TGA) and size range of the MSAH-functionalized $BaSO_4$ nanoparticles.

Sample code	Molar ratio of MSAH/$BaCl_2$	Mass ratio of MSAH/$BaSO_4$	Mass loss of $BaSO_4$	Particle size range(nm)
S1	0	0	0.0247	100-500
S2	0.016	0.013	0.0316	20-30
S3	0.032	0.026	0.0316	10-20
S4	0.064	0.052	0.031	20-30
S5	0.128	0.108	0.038	100-300

AMSA are both spherical and platelet-like with a broad size distribution from 200 – 1000 nm (Figure 9g). With the molar ratio increased to 0.008, 0.016, and 0.032, the size of the particles decreases to 200 – 300 nm (Figure 9h-j). With the further increased molar ratio, the particle size increases to 300 – 500 nm (Figure 9k-l).

The results above demonstrate limited morphology control capability of SMPS and AMSA under the explored conditions. Compared to MSAH, both SMPS and AMSA only possess negatively charged functional group in aqueous solution. As a result, electrical shield layer is hardly formed on the surface functionalized $BaSO_4$ particles. Consequently, the growth of the $BaSO_4$ particles cannot be effectively inhibited by SMPS and AMSA, leading to the formation of large sized $BaSO_4$ particles.

Surface Modification Content and Crystallographic Phase of the Surface Functionalized $BaSO_4$ Particles

The content of the surface modification agent coated on the $BaSO_4$ particle surface is qualitatively characterized by FTIR. **Figure S2** shows the FTIR spectrum of the particles synthesized with different types (MSAH, SMPS, and AMSA) and amounts of modification agents (molar ratio of surface modification agent over $BaCl_2$ varied from 0 to 0.128). Compared to the bare $BaSO_4$ particles, the FTIR absorbance at 1375 cm^{-1}(deformation bending of CH_3) and 1630 cm^{-1} (stretching of C=C) proves successful coating of surface modification agents on the particle surface. The amount of MSAH coated on the $BaSO_4$ particle surface is quantitatively determined by thermo gravimetric analysis (TGA) **(Table 2** and **Figure S3)**. Because the temperature ranges of the mass loss of water and MSAH are partially overlapped, it is hard to determine the actual mass loss of MSAH directly. Without MSAH coating, the mass loss ratio of 0.025 is ascribed to the residual water on the $BaSO_4$ nanoparticle surface[36]. With the molar ratio of MSAH/$BaCl_2$ increased from 0.016 to 0.064 (S2 to S4), the corresponding theoretical mass loss ratio is increased from 0.013 to 0.052. However, the apparent mass loss determined by TGA is kept at around 0.032 and the actual amount of MSAH coated on the $BaSO_4$ particles is deduced to be around 0.007. Only when the molar ratio is increased to 0.128, the actual amount of MSAH coating is slightly increased to 0.013 (Table 2). It indicates that only part of MSAH is coated on the $BaSO_4$ particle surface.

The effect of surface modification agent on the crystallographic phase of the $BaSO_4$ particle is investigated by x-ray diffraction (XRD). It is necessary to identify the crystallographic structure of the $BaSO_4$ particles because different crystallographic modifications may influence the x-ray radiopacity. **Figure S4** shows that the XRD patterns of the particles functionalized with MSAH, SMPS, and AMSA are all consistent with typical orthorhombic (JCPDS 80-0512). It indicates that the use of surface phase of $BaSO_4$ modification agents only change the morphology and surface functionality of the particles, but not modify the crystallographic phase of the particles.

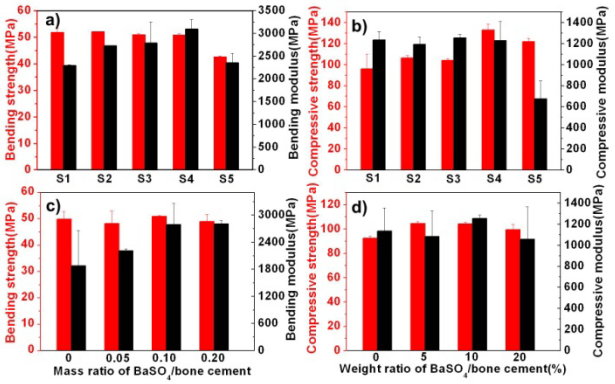

Figure 10. Mechanical properties of the PMMA bone cements containing different types of $BaSO_4$ nanoparticles. a) Bending strength (red) and modulus (black) of the bone cements containing the $BaSO_4$ particles synthesized with different molar ratios of MSAH/$BaCl_2$, b) Compressive strength (red) and modulus (black) of the bone cements containing the $BaSO_4$ particles synthesized with different molar ratios of MSAH/$BaCl_2$, c) Bending strength (red) and modulus (black) of the bone cements containing different amounts of $BaSO_4$ nanoparticles, d) Compressive strength (red) and modulus (black) of the bone cements containing different amounts of $BaSO_4$ nanoparticles.

Mechanical Properties of the Bone Cements Containing MSAH Functionalized $BaSO_4$ Nanoparticles

The influence of the MSAH functionalized $BaSO_4$ nanoparticles on the mechanical properties of the PMMA bone cements is investigated. Critical mechanical properties including bending properties and compressive properties are characterized (**Figure 10**). Compared to the bare $BaSO_4$ particles (S1 in Table 2), the use of MSAH effectively improves the bending modulus of the bone cement from 2293 MPa (S1) to 3100 MPa (S4), which is likely due to the decreased particle size and increased MSAH coating (right column in Figure 10a). However, the bending modulus decreases to 2358 MPa with S5, probably due to the increased particle size. Compared to bending modulus, the bending strength does not show significant change from S1 to S4 (left column in Figure 10a). Figure 10b shows that the compressive strength is gradually increased from 96 MPa (S1) to 132 MPa (S4) due to increased amount of MSAH coating and decreased particle size (left column). Regarding compressive modulus, it shows similar results at about 1200 MPa from S1 to S4 (right column).

The influence of different amounts of MSAH functionalized $BaSO_4$ nanoparticles on the mechanical properties of the bone cements are also investigated using S2 as demonstration. Figure 10c shows that with increasing amount of particles, the bending modulus is significantly increased from 1878 MPa (0 wt. % of $BaSO_4$) to 2803 MPa (20 wt. % of $BaSO_4$). However, the bending strength does not show significant change with increasing loading of the particles, which maintains at about 50 MPa. Figure 10d shows that the compressive strength is effectively increased from

Table 3. Radiopacity of the bone cements containing different amounts (0 wt. % - 20 wt. %) of BaSO4 particles (coated with 1.3 wt. % of MSAH), and different types (S1-S5) of BaSO4 particles with 5 wt. % of BaSO4 as indicated by transmission light value. Smaller transmission light value indicates better radiopacity.

Sample	Transmission light value	Standard deviation
Air	12882	399
0 wt. %$BaSO_4$ (S2)	11451	425
5 wt. %$BaSO_4$ (S2)	10099	1408
10 wt. %$BaSO_4$ (S2)	8092	1596
20 wt. %$BaSO_4$ (S2)	6992	1724
S1(10 wt. %$BaSO_4$)	7687	1534
S2(10 wt. %$BaSO_4$)	8092	1596
S3(10 wt. %$BaSO_4$)	8535	1601
S4(10 wt. %$BaSO_4$)	8986	1420
S5(10 wt. %$BaSO_4$)	8503	1431

90 MPa (0 wt. % of $BaSO_4$) to 100 MPa (5 wt. % and 10 wt. % of $BaSO_4$), while slightly decreases to around 95 MPa (20 wt. % of $BaSO_4$).

It is reported that the introduction of radiopacifier filler such as $BaSO_4$ particles decreases the bending strength and compressive strength of the bone cements significantly[37]. However, here the MSAH functionalized $BaSO_4$ nanoparticles do not deteriorate and even improve the mechanical properties of the bone cements. This is likely due to the decreased $BaSO_4$ particle size, improved compatibility and enhanced interaction between the $BaSO_4$ particle and the PMMA matrix.

X-ray Radiopacity of Bone Cements

The radiopacity of the bone cements containing different types and amounts of MSAH-functionalized $BaSO_4$ particles is studied (**Table 3**). The bone cement without $BaSO_4$ exhibits poor radiopacity, which is similar to air. With increasing loading of the particles from 0 wt. % to 20 wt. % (sample S2), the radiopacity is significantly improved, as indicated by the dramatic decrease of the TLV (transmission light value) from 11451 to 6992.However, the TLV of the bone cements containing different types of particles (S1 to S5) with the same mass ratio (10 wt. %) only change slightly. Considering that the TLVs are sensitive to the local scanned spots of the samples and the standard deviations are quite large compared to the averaged TLVs, it is reasonable to say that the use of different types of MSAH functionalized $BaSO_4$ particles addressed in this study do not change the radiopacity of the bone cements significantly.

***In Vitro* Biocompatibility of Bone Cements**

The influence of the type and amount of MSAH-functionalized $BaSO_4$ nanoparticles on the in vitro biocompatibility of the bone cements is studied. **Figure 11a** summarizes the density of osteoblast cell on the bone cement surface composed of different types of particles. Compared to the bone cement containing bare $BaSO_4$ particles (S1), the cell density is significantly increased when the MSAH-functionalized $BaSO_4$ nanoparticles are used as fillers ($p<0.005$ for comparing S2-S5 with S1). These results indicate that the MSAH-functionalized $BaSO_4$particles improve the biocompatibility of the bone cements. Concerning the bone

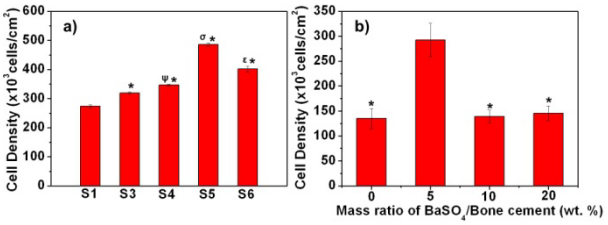

Figure 11. Cell density of the human osteoblast cells seeded for 24 hours on the bone cements containing different types (S1-S6, Fig 7a) and different amounts (0 wt. %-20wt. %, Fig 7b) of the $BaSO_4$ particles (S2). Data=mean ± SEM; N=3. *Compared to 0 % mass ratio of MSAH/$BaCl_2$ (S1), adhesion on bone cements containing MSAH coated $BaSO_4$ nanoparticles is found to be greater (the mass ratio of MSAH/$BaCl_2$): 1.3 wt. % (S2) MSAH ($p<0.005$), 2.6 wt. % (S3) MSAH ($p<0.005$), 5.2 wt. % (S4) MSAH ($p<0.001$), 10.4 wt. % (S5) MSAH in $BaSO_4$ ($p<0.001$). ΨAdhesion bone cement containing S3 was observed to be greater than cements containing S2 ($p<0.02$) and fewer than cements containing S4 ($p<0.001$). Compared to cements containing S4, the adhesion on cements containing S5 was found to be greater ($p<0.005$). *Compared to 5 % mass ratio of $BaSO_4$/bone cement, adhesion on bone cements containing $BaSO_4$ nanoparticles was found to be fewer: 0 wt. % $BaSO_4$ ($p<0.005$) , 10 wt. % $BaSO_4$ ($p<0.05$) and 20 wt. % $BaSO_4$ ($p<0.05$).

cements containing different types of particles, the osteoblast density on cements gradually increases from S2 to S4, while slightly decreases with S5. The results imply that the use of MSAH-functionalized $BaSO_4$ nanoparticles improves the in vitro biocompatibility of the bone cements.

The in vitro biocompatibility of the bone cements containing different mass ratios of MSAH-functionalized $BaSO_4$ nanoparticles (S2) is summarized in **Figure 11b.** It shows that with 5 wt. % of S2, maximum osteoblast cell density is reached. While with further increased mass ratios（10 wt. % and 20 wt. % of S2）, the cell density is decreased, but still comparable to the bone cement without $BaSO_4$. It indicates that the use of MSAH-functionalized $BaSO_4$ nanoparticles does not hurt and even improve the biocompatibility of the bone cements with certain composition.

As a complementary study, the confocal images of the human osteoblast cells cultured on the bone cements are presented in **Figure 12**.The adhesion of the cells is least on the bone cement containing bare $BaSO_4$ particles (S1, Figure 12a). From S2 to S5, the adhesion of the cells gradually increases (Figure 12b-e). Particularly, a sharp increase of adhesion is observed from S3 to S4 and S5 (Figure 12c-e). The results confirm that the MSAH-functionalized $BaSO_4$ nanoparticles promote the osteoblast adhesion and proliferation on the bone cement surface. Concerning the cements containing different amounts (0 wt. % - 20 wt. %) of particles (S2), the confocal images do not show significant difference (Figure 12f-i). It indicates that the use of MSAH-functionalized $BaSO_4$ nanoparticles do not deteriorate the biocompatibility of the bone cements.

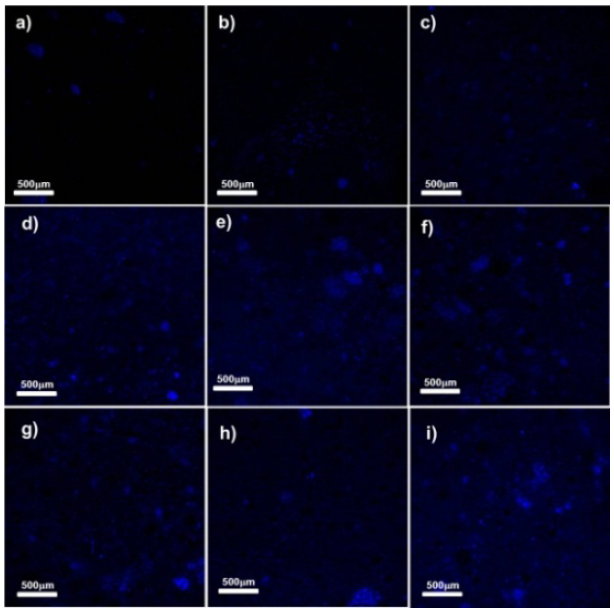

Figure 12. Confocal laser scanning microscope fluorescence images of the human osteoblast cells seeded for 24 hours on the bone cement surface containing different types (a-e: S1-S5) $BaSO_4$ particles (10 wt.%) and different amounts (f-i: 0 wt. %, 5 wt. %, 10 wt. %, and 20 wt. % respectively) of the $BaSO_4$ nanoparticles (S2).

Conclusion

In conclusion, a new strategy has been developed to synthesize surface functionalized $BaSO_4$ nanoparticles in a controllable way. Pre-decomposition of $K_2S_2O_8$ under mild condition to generate SO_4^{2-} *in situ* is combined with a new difunctional surface modification agent (MSAH). By systematically varying the pre-decomposition time and molar ratio of MSAH/$BaCl_2$, the nucleation and particle growth of $BaSO_4$ are well tuned. As a result, spherical MSAH-functionalized $BaSO_4$ nanoparticles with the size down to 10 nm are synthesized. The applicability of this strategy on other surface modification agents (SMPS and AMSA) is investigated. The use of MSAH-functionalized $BaSO_4$ nanoparticles effectively improves the bending modulus and compressive strength of the bone cements, while not deteriorate the bending strength and compressive modulus of the bone cements. The x-ray radiopacity of the bone cements containing different types and amounts of MSAH-functionalized $BaSO_4$ nanoparticles are characterized. The results show that with increasing loading of the MSAH-functionalized $BaSO_4$ nanoparticles from 0 wt. % to 20 wt. %, the radiopacity of the bone cements is significantly improved. However, when different types of MSAH-functionalized $BaSO_4$ particles are applied with the same mass ratio in bone cements, the radiopacity do not change significantly. The *in vitro* biocompatibility of the bone cements consisting of different types and amounts of MSAH-functionalized $BaSO_4$ particles are also investigated. The density of the human osteoblast cells is significantly improved with increasing MSAH coating and decreased particle size. The increasing loading of the MSAH-functionalized $BaSO_4$ nanoparticles from 0 wt. % to 20 wt. % does not deteriorate the biocompatibility of the bone cements.

Acknowledgements

This research is funded by the Natural Science Foundation of China (21004074, 51103172, 212101064), the Hundred Talents Program of the Chinese Academy of Sciences (J.F.), the Ningbo Natural Science Foundation (2011A610120, 2012A610176), the Zhejiang Nonprofit Technology Applied Research Program (2013C33190), the Zhejiang Natural Science Foundation of China (LR13B040001, LQ13E030005), the Program for Ningbo Innovative Research Team (2009B21008, 2012B82019), Ningbo Key Laboratory of Polymer Materials, and the Scientific Research Foundation for the Returned Overseas Chinese Scholars, State Education Ministry (J.F.).

Notes and references

[a] *Polymers and Composites Division, Ningbo Institute of Materials Technology and Engineering, Chinese Academy of Sciences, 519 Zhuangshi Rd, Zhenhai District, Ningbo, Zhejiang Province, 315201, P. R. China. Email: fujun@nimte.ac.cn, chengyj@nimte.ac.cn*
[b] *Faculty of Materials Science and Chemical Engineering, Ningbo University, Ningbo, Zhejiang Province, 315211, P. R. China.*
[c] *Department of Radiology, Nanjing Drum Tower Hospital, the Affiliated Hospital of Nanjing University Medical School, 321 Zhongshan North Rd, Nanjing, Jiangsu Province, 210008, P. R. China. Email: zhoukefeng1977@163.com*
[d] *School of Chemical Engineering, Ningbo University of Technology, Ningbo, Zhejiang Province, 315016, P. R. China*

† Electronic Supplementary Information (ESI) available: [pH evolution against reacation time, FTIR, XRD, and TGA of the surface functionalized $BaSO_4$ particles,]. See DOI: 10.1039/b000000x/

1. Ghashang and Majid, *Curr. Org. Synth.*, 2012, **9**, 727-736.
2. F. Li and G. Yuan, *Chem.Commun.*, 2005, 2238-2240.
3. O'Conner.S.D and Summers.R.M, *Acad. Radiol.*, 2007, **14**, 72.
4. M.-H. Qu, Y.-Z. Wang, C. Wang, X.-G. Ge, D.-Y. Wang and Q. Zhou, *Eur. Polym. J.*, 2005, **41**, 2569-2574.
5. J. Lin and H.-W. Gao, *J. Mater. Chem.*, 2009, **19**, 3598.
6. I. C. Romero-Ibarra, G. Rodriguez-Gattorno, M. F. Garcia-Sanchez, A. Sanchez-Solis and O. Manero, *Langmuir*, 2010, **26**, 6954-6959.
7. N. Nandakumar and P. Kurian, *Powder. Technol.*, 2012, **221**, 51-56.
8. C. I. Vallo, T. R. Cuadrado and P. M. Frontini, *Polym. Int.*, 1997, **43**, 260-268.
9. C. I. Vallo, *J. Biome. Mater. Res. Part B*, 2000, **53**, 717-727.
10. B. Niemann, P. Veit and K. Sundmacher, *Langmuir*, 2008, **24**, 4320-4328.
11. G. M. Sylvain, S. Kassab, R. Coutts and R. Santore, *The Journal of arthroplasty*, 2001, **16**, 141-148.
12. S. Beck and A. Boger, *Acta. Biomater.*, 2009, **5**, 2503-2507.
13. B. SK and G. LN, *J. Biomed. Mater. Res.*, 1995, **29**, 233-237.
14. G. Lewis, J. Xu, S. Madigan and M. R. Towler, *Acta. Biomater.*, 2007, **3**, 970-979.
15. P. E. Sinnett-Jones, M. Browne, A. J. Moffat, J. R. Jeffers, N. Saffari, J. Y. Buffiere and I. Sinclair, *J. Biomed. Mater. Res.. Part A*, 2009, **89**, 1088-1097.
16. M. P. Ginebraa, L. Albuixecha, E. Fern!andez-Barragana, F. J. G. C. Aparicioa, J. S. Romanb, B. Vazquezb and J. A. Planella, *Biomaterials*, 2002, **23**, 1773-1882.
17. S. M. Kurtz, M. L. Villarraga, K. Zhao and A. A. Edidin, *Biomaterials*, 2005, **26**, 3699-3712.
18. N. Shearwood-Porter, M. Browne and I. Sinclair, *J. Mech. Behav. Bimed.*, 2012, **13**, 85-92.

19. R. Ormsby, T. McNally, P. O'Hare, G. Burke, C. Mitchell and N. Dunne, *Acta. Biomater.*, 2012, **8**, 1201-1212.
20. P. A. Tran, L. Sarin, R. H. Hurt and T. J. Webster, *J. Mater. Chem.*, 2009, **19**, 2653.
21. B. P. Bastakoti, S. Guragain, Y. Yokoyama, S.-i. Yusa and K. Nakashima, *New. J. Chem.*, 2012, **36**, 125-129.
22. Z. Shi, K. G. Neoh, E. T. Kang and W. Wang, *Biomaterials*, 2006, **27**, 2440-2449.
23. A. Ricker, P. Liu-Snyder and T. J. Webster, *Int. J. Nanomedicine.*, 2008, **3**, 125-132.
24. R. Gillani, B. Ercan, A. Qiao and T. J. Webster, *Int. J. Nanomedicine.*, 2010, **5**, 1-11.
25. H. Zhang, Y. Liu, J. Zhang, H. Sun, J. Wu and B. Yang, *Langmuir*, 2008, **24**, 12730-12733.
26. M. Uchida, A. Sue, T. Yoshioka and A. Okuwaki, *CrystEngComm*, 2001, **5**, 1-6.
27. X.-H. Zhang, F.-W. Yan, C.-Y. Guo, F.-B. Li, Z.-J. Huang and G.-Q. Yuan, *CrystEngComm*, 2012, **13**, 5267-5273.
28. A. May-Pat, W. Herrera-Kao, J. V. Cauich-Rodriguez, J. M. Cervantes-Uc and S. G. Flores-Gallardo, *J. Mech. Behav. Biomed.*, 2012, **6**, 95-105.
29. H. Bala, W. Fu, Y. Guo, J. Zhao, Y. Jiang, X. Ding, K. Yu, M. Li and Z. Wang, *Colloids. Surf., A*, 2006, **274**, 71-76.
30. M. Li, H. Cölfen and S. Manna, *J. Mater. Chem.*, 2004, **14**, 2269-2276.
31. F. Wang, G. Xu, Z. Zhang and X. Xin, *Colloids Surf., A*, 2005, **259**, 151-154.
32. Q. Chen and X. Shen, *Cryst. Growth Des.*, 2010, **10**, 3838-3842.
33. Q. Chen, X. Shen and H. Gao, *Adv. Colloid. Interface. Sci.*, 2010, 32-44.
34. S.-W. Kuo, Y.-C. Chung, K.-U. Jeong and F.-C. Chang, *J. Phys. Chem. C*, 2008, **112**, 16470-16477.
35. C. Fang, F. Hua, Y. Cong, J. Fu and Y.-J. Cheng, *J. Mater. Chem. B*, 2013, **1**, 4043-4047.
36. Z.-W. Sun, Q.-F. An, Q. Zhao, Y.-G. Shangguan and Q. Zheng, *Cryst. Growth Des.*, 2012, **12**, 2382-2388.
37. R. A, L.-S. P and W. TJ, *Int. J. Nanomedicine.*, 2008, **3**, 125-132.